Fractal Scale Effect in Quasi-Brittle Materials Using a Version of the Discrete Element Method

fractal and fractional

MDPI

Article

Fractal Scale Effect in Quasi-Brittle Materials Using a Version of the Discrete Element Method

Luis Eduardo Kosteski [1,*], Leandro Ferreira Friedrich [1], Matheus Machado Costa [1], Caroline Bremm [1], Ignacio Iturrioz [2], Jie Xu [3] and Giuseppe Lacidogna [4]

[1] Modeling and Analysis Experimental of Composites Group, Engineering Post Graduation Program, Federal University of Pampa, Alegrete Campus, Av. Tiaraju 810, Alegrete 97546-550, Brazil; leandrofriedrich@unipampa.edu.br (L.F.F.); matheuscosta.aluno@unipampa.edu.br (M.M.C.); carolinebremm.aluno@unipampa.edu.br (C.B.)
[2] Applied Mechanical Group GMAP, Mechanical Engeneering Post Graduation Program, Federal University of Rio Grande do Sul, Rua Sarmento Leite, 425, Porto Alegre 90040-001, Brazil; ignacio.iturrioz@ufrgs.br
[3] Key Laboratory of Earthquake Engineering Simulation and Seismic Resilience of China Earthquake Administration, School of Civil Engineering, Tianjin University, Tianjin 300350, China; jxu@tju.edu.cn
[4] Department of Structural, Geotechnical and Building Engineering, Politecnico di Torino, 10129 Turin, Italy; giuseppe.lacidogna@polito.it
* Correspondence: luiskosteski@unipampa.edu.br

Abstract: In engineering applications, it is crucial to consider the size dependence of a material's mechanical properties and its overall behavior. One of the theories that quantifies this phenomenon in quasi-brittle materials is the cohesive fractal theory (CFT) introduced by Carpinteri and his collaborators. This theory describes the behavior of materials using fractal dimensions. To investigate whether the scale effect can be analyzed using the CFT, a version of the Lattice Discrete Element Method (LDEM) is employed. The accuracy of the LDEM in capturing the scale effect is evaluated through simulations of three primary tests. Specifically, rock specimens are subjected to tensile, compressive, and bending loads to determine their mechanical properties. The influence of material heterogeneity and boundary conditions is also examined. In scenarios involving tensile and bending loads, the localization of a significant crack leads to failure. According to the CFT, the sum of the fractal exponents is close to unity, with values of 1.0 (mean value) for tensile loading and 0.97 for bending loading. However, the compressive loading results do not exhibit this characteristic, as no single prominent crack leads to failure. Overall, the LDEM results are consistent with the CFT, effectively quantifying the scale effect without modifying the elementary constitutive law.

Keywords: quasi-brittle materials; scale effect; lattice discrete element method

Citation: Kosteski, L.E.; Friedrich, L.F.; Costa, M.M.; Bremm, C.; Iturrioz, I.; Xu, J.; Lacidogna, G. Fractal Scale Effect in Quasi-Brittle Materials Using a Version of the Discrete Element Method. *Fractal Fract.* **2024**, *8*, 678. https://doi.org/10.3390/fractalfract8120678

Academic Editor: Carlo Cattani

Received: 24 September 2024
Revised: 10 November 2024
Accepted: 19 November 2024
Published: 21 November 2024

1. Introduction

Quasi-brittle materials, including concrete, ceramics, and natural rocks, do not flow; rather, they undergo gradual deterioration as microstructural bonds are broken under increasing or cyclic loading. The primary damage mechanism involves the nucleation and growth of microcracks. It is important to note that under tensile stress, cracks typically form perpendicular to the stress direction [1–3]. Materials with brittle or quasi-brittle behavior exhibit changes in strength depending on the size of the structure being analyzed. Therefore, it is essential to quantify this scale effect to ensure the appropriate ultimate strength values are used in structural design and sizing.

Conducting experiments at different scales is only sometimes feasible due to the cost, element size, equipment availability, or the time required to obtain the data. Therefore, computational tools are invaluable for designers and researchers, as they are less expensive in terms of time and laboratory resources.

In recent years, there has been a notable expansion in the use of computational techniques for the study of fracture phenomena, which has contributed to the available experimental data. Classical approaches such as continuum mechanics have been modified to accommodate the emergence of cracks in the modeled solid. Notable examples include the Cohesive Zone Model (CZM) [4,5] and the robust extended finite element method (XFEM) [6]. Another approach is the Phase Field Method (PFM) [7,8], which uses a continuous variable to represent the transition between damaged and undamaged phases. While PFM avoids the need for crack tracking, it generally requires very fine meshes. It is favored for its relatively straightforward numerical implementation and its ability to represent complex crack processes such as initiation, propagation, and branching [9]. Additionally, another approach that has emerged from continuum mechanics is the so-called Peridynamics (PD) proposed by Silling [10]. PD is a nonlocal method in which the solid is modeled as a system of nodes with mass connected by interaction functions that represent stiffness. Recently, this method has been applied to quasi-brittle materials and their properties [11–13].

An additional class of methods that aim to move away from the restrictions of those methods based on continuum mechanics are the Discrete Element Methods. In these methods, the solid is represented as an arrangement of uniaxial elements (such as trusses and beams [14,15]) with the mass concentrated at the end nodes, and they are able to take into account the random nature of the material properties [16]. This is the case of the Lattice Discrete Element Method (LDEM) used in this study. The LDEM has the advantage of being able to study the damage process in detail, such as crack initiation, crack interactions, and the ability to capture the effect of scale (see, for example, [17–19]). The LDEM employs a simple bilinear constitutive law, where the parameters to be defined are easy to compute and interpret. In this sense, the results are aligned with the fractal theory that explains the emergence of the dependence of the mechanical properties on structural size and, therefore, is a numerical tool to be explored in this paper.

This work uses the LDEM to analyze the size effect on rock specimens subjected not only to tensile loading, as in previous works [18,19], but also to flexural and compressive loadings. The elements in the LDEM's formulation consider only the damage under tension, whereas a linear elastic behavior is assumed under compression. In such a case, the compression failure occurs indirectly through tensile stress. Therefore, to assess the efficacy of this method, it is essential to conduct a comprehensive examination of the behavior of the elements under diverse loading conditions. Moreover, the influence of the correlation lengths on the random field for the fracture energy, employed to consider the material's heterogeneity and the boundary conditions, is examined.

The paper is structured as follows. Section 2 presents the theoretical concepts of the cohesive fractal model, which are essential for understanding and analyzing the numerical results. Section 3 provides an overview of the fundamental principles of the Lattice Discrete Element Method (LDEM), while Section 4 discusses the implementation of the theoretical formulation of the LDEM within the Abaqus/Explicit 6.13 software environment. Section 5 is dedicated to the numerical simulation of the size effect on rock specimens subjected to tensile, flexural, and compressive loads. Section 6 presents the results of these numerical simulations and offers a thorough discussion of the findings. The main conclusions are summarized in Section 7.

2. The Cohesive Fractal Theory

Carpinteri and co-workers [20–24] proposed that fractal geometry offers a unified explanation for the scale effects on the tensile and compressive properties of quasi-brittle materials, which would otherwise be difficult to achieve. They defined the fractal cohesive and fractal overlapping laws and validated the fractal approach for a more general interpretation of the scale effects [25].

Through the concept of fractal dimensions proposed by Mandelbrot [26], Carpinteri et al. [21] introduced a fractal cohesive model that is independent of structural size. As discussed

in [18,19], among others, to achieve this purpose, three material parameters, the tensile strength σ_u, the fracture energy G_f, and the critical strain ε_c, must be defined in a non-conventional form, known as fractal tensile strength ${\sigma_u}^*$, fractal fracture energy ${G_f}^*$, and fractal critical strain ${\varepsilon_c}^*$.

The fractal tensile strength ${\sigma_u}^*$ is a scale-invariant material parameter with anomalous physical dimensions $[F][L]^{-(2-d_\sigma)}$. The nominal value σ_u is subjected to the scale effect described by the following negative power law [20]:

$$\sigma_u = \sigma_u^* b^{-d_\sigma} \tag{1}$$

The exponent d_σ of this power law can vary between 0, corresponding to the homogeneous regime (large scale), and 0.5, corresponding to the fractal regime (small scale).

The critical elongation w_c can expressed as

$$w_c = \varepsilon_c^* b^{(1-d_\varepsilon)} \tag{2}$$

where ε_c^* is also a true scale-invariant material parameter with anomalous physical dimension $[L]^{(d_\varepsilon)}$. Once the test specimen has reached its maximum tensile strength, $w = w_c$. The fractal exponent d_ε indicates the disorder in the mesoscopic damage process, ranging from 1 in the homogeneous regime (large scale) to 0 in the fractal regime (small scale).

Finally, the nominal value G_f is subjected to a scale effect described by the following positive power law:

$$G_f = G_f^* b^{d_G} \tag{3}$$

The fractal fracture energy G_f^* is the true scale-invariant material parameter with anomalous physical dimensions $[FL][L]^{-(2+d_G)}$. Carpinteri and co-workers (see, for example, [22,24]) explain that the fractal domain has dimensions between 3 and 2. This fractal domain can be considered as $2 + d_G$; then, the exponent d_G ranges between 1 and 0 in the homogeneous regime, large scale.

The total work performed by the system can be represented through the area of the stress-crack opening or the displacement (w) curve. This area is also the value of G_f, i.e., the sum of all energies involved in the sample rupture process [21,27,28]. From this,

$$G_f = \int_0^{w_c} \sigma dw = b^{1-d_\sigma-d_\varepsilon} \int_0^{\varepsilon_c^*} \sigma^* d\varepsilon^* = G_f^* b^{1-d_\sigma-d_\varepsilon} \tag{4}$$

It is obtained that the fundamental relationship between the scale exponents is given by

$$d_\sigma + d_\varepsilon + d_G = 1 \tag{5}$$

This fractal exponent varies depending on the specimen's geometric shape, the type of failure (tensile or bending test), and the characteristics of the concrete, such as maximum aggregate size and component quantities. Experimentally, it is found that the fractal exponent for tensile stress varies between 0.091 and 0.41, the fractal exponent for fracture energy between 0.085 and 0.48, and the fractal exponent for strains between 0.48 and 0.73 [18–20,23,27,29–32].

Carpinteri and co-workers [25,33] applied the previously discussed fractal approach for the tensile behavior to develop a scale-independent fractal overlapping law. They also mentioned that experimental tests conducted across large scale ranges clearly show that compressive strength decreases with increasing specimen size (see [34,35]). Similarly, the dissipated energy density decreases as specimen size increases (see [36]). They noted that energy dissipation occurs not within a volume but rather within a fractal domain whose dimension lies between those of a surface and a volume. In their work, they did not consider the size effects on compressive strength because this mechanical property shows

statistical dispersion without a clear trend. Consequently, the exponent $d\sigma$ in Equation (1) is taken as 0, and, therefore, Equation (5) becomes

$$d_\varepsilon + d_G = 1 \tag{6}$$

Analyzing the results of Ferrara and Gobbi (see [37]), they found the exponent dG in Equation (3) to be 0.27, indicating that the energy dissipation occurs within a fractal domain of dimension 2.27. Meanwhile, the exponent d_ε= 0.73, according to Equation (9), implies that the deformation is neither localized in a single section nor uniformly distributed over the specimen's length.

For three-point bending specimens, the tensile strength varies similarly to tensile loading (see Equation (1)) as presented by [38,39]. To determine the scale effect on the fracture energy, it is first necessary to calculate the dissipated energy (W), represented by the area under the F– δ diagram, where δ is the displacement of the loading point. G_f is the ratio of the dissipated energy to the ligament area, in this case, the beam's cross-section. In this case, the fractal kinematic parameter considered, which corresponds to the critical displacement in a tensile test, is the localized rotation at the beam mid-span. This parameter, at the point of failure, is defined as

$$\varphi_c = \frac{\delta_c}{S/2} \tag{7}$$

where S is the span length, and δ_c is the mid-span displacement [38]. The power law describing the scale effect of the kinematic parameter for the TPB test is given by

$$\varphi_c = \varphi_c^* b^{-d\chi} \tag{8}$$

where $d\chi$ is the fractal exponent of the rotation found through the bi-logarithm diagram. Carpinteri and Accornero [38] found the exponent $d\chi$ for the experimental case to be 0.343. They also explained that the kinematic parameter ranges between the dimension of the rotation angle $[S]^0$ and a curvature $[S]^1$. That is, the parameter shifts from a generalized displacement to a deformation. From the fractal perspective, the decrease in the kinematic parameter represents the curvature within the beam span as a lacunar fractal characterized by infinite radial cracks converging toward the center of curvature. Since a rotation angle is dimensionless, a radius of curvature has the dimension $[S]^1$, while curvature has the dimension $[S]^{-1}$; therefore, the inverse of the renormalized critical rotation returns the renormalized critical curvature, χ_c^* [39].

Similar to Equation (5), for tensile scale effect, the renormalization of fracture energy provides the fundamental relationship between the fractal exponents [38]:

$$d\sigma + d\chi + dG = 1 \tag{9}$$

In three-point bending tests, the exponent values reported by Carpinteri and Accornero [38] and Lacidogna et al. [39] fall within the ranges of 0.1 to 0.3 for flexural strength, 0.1 to 0.3 for fracture energy, and 0.2 to 0.5 for the kinematic parameter.

The theory presented above, along with Equations (1)–(9), is explained in detail in several papers, some of which that have already been referenced in this work. These include, for example, papers [29,30,38].

3. The Lattice Discrete Element Method

3.1. Model Description

Riera [40] proposed the LDEM version, in which the continuum medium is represented by a cubic arrangement of uniaxial elements. The mass of the body is concentrated at the nodes of this arrangement. Every node has three degrees of freedom, representing the displacement in one of the three orthogonal directions, all defined by the Cartesian system. Figure 1a presents the basic cubic module of the LDEM. The longitudinal elements have a

length L_l (blue in Figure 1a), equal to the cubic model side L, whereas the diagonal elements (red in Figure 1a) have a relative length $L_d = L\sqrt{3}/2$.

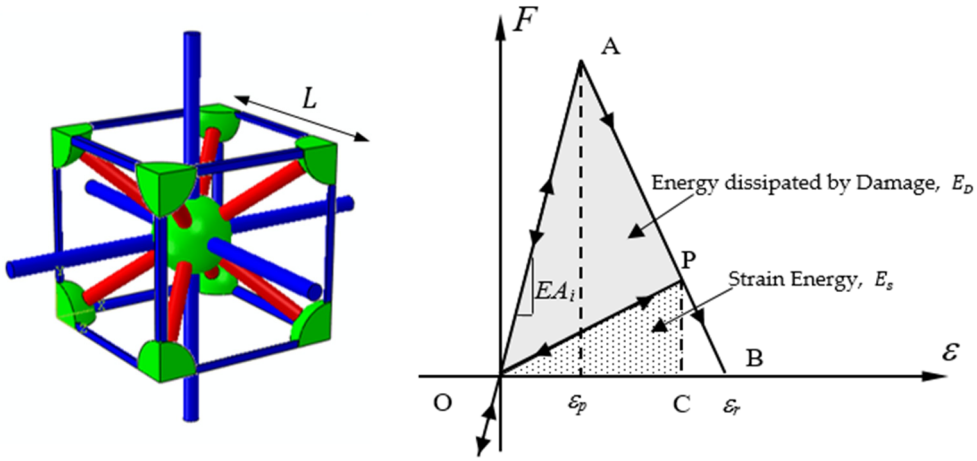

(**a**) (**b**)

Figure 1. (**a**) Basic LDEM cubic module and (**b**) elementary constitutive relationship.

The cross-sectional area of the elements, as shown in Figure 1a, which are needed to maintain the same properties for the discretized model and a continuous isotropic elastic solid, are defined as follows:

$$A_l = \frac{1}{2(1+\nu)}L^2,\ A_d = \frac{3\sqrt{3}}{2}\frac{\nu}{(1-2\nu)}A_l \tag{10}$$

where ν is the Poisson's ratio of the selected material and A_l and A_d are the area of the longitudinal and diagonal elements, respectively. Notably, to obtain an exact correspondence between the isotropic continuum and its equivalent discrete model, the Poisson ratio must be equal to 0.25. However, discrepancies in expected values arise in the shear terms when $\nu \neq 0.25$.

The energy generated in the fracture of a continuum and an LDEM model must be equivalent. Then, to guarantee this compatibility, the equivalent fracture area of the element is defined as $A_i^*/A_i = 0.3474$ [18,41,42].

The second law of Newton, expressed in Equation (11), is used to determine the global system behavior. This equation is integrated for each node at each time increment.

$$M\ddot{u} + C\dot{u} + F(t) - P(t) = 0 \tag{11}$$

In Equation (11), the mass matrix M and the damping matrix C are both diagonal. For this reason, the equation can be decoupled and solved efficiently using explicit schemes such as the Central Finite Difference Method in order to obtain the vector of nodal displacements u and its time derivatives. The force balance of Equation (11) also considers the element's stiffness, with the vector $F(t)$ representing the nodal internal forces and the vector $P(t)$ representing the nodal external forces. This equation is directly integrated at each time increment, naturally and efficiently accounting for large displacements [42].

The stress wave propagation in the elements of LDEM discretization can occur only along its length because they are uniaxial. Consequently, the maximum time integration increment, Δt_{max}, is constrained by this effect. Then, the elements with the shortest length, which are the diagonal elements in the LDEM, determine the shortest propagation time for a wave. For maintaining the numerical stability of the system, the relationship between

the maximum time increment and the element's length is crucial, as expressed by the Courant–Friedrichs–Lewy (CFL) criterion [43]. This criterion is presented in Equation (12),

$$\Delta t_{max} \leq L_d / C_L, \tag{12}$$

where C_L represents the velocity of the longitudinal wave of the medium and is equal to $C_L = \sqrt{E/\rho}$ for solid materials. In this equation, E is Young's modulus and ρ is the mass density.

3.2. LDEM Constitutive Model

The anisotropic damage law for concrete implemented in the LDEM is based on Hillerborg's approach [44]. This relationship defines a bilinear law that correlates the element's tensile force, F, and strain, ε (see Figure 1b). This law accounts for the irreversible damage caused by crack initiation, coalescence, and propagation.

The maximum strain before the onset of damage is called critical strain, ε_p, as shown in Figure 1b. For $\varepsilon \leq \varepsilon_p$ the unloading process is linear up to the origin. However, if $\varepsilon \geq \varepsilon_p$ occurs, the unloading occurs happens at a reduced slope, reflecting the loss of stiffness due to damage. The critical strain, ε_p, is as follows:

$$\varepsilon_p = \sqrt{\frac{G_f}{E d_{eq}}} \tag{13}$$

where G_f is the value of the mean fracture energy related to the length of the LDEM basic module adopted, L. The parameter d_{eq} is a characteristic length of the material similar to the width of the plasticity region at the crack tip in the Dugdale model.

The area under the curve represents the density energy necessary to break the element, and it is defined using the relationship between the fracture energy, G_f (material property), and the characteristics of the model in the LDEM, as follows:

$$\int_0^{\varepsilon_r} \sigma(\varepsilon) d\varepsilon = \frac{G_f A_i^*}{L_i A_i}. \tag{14}$$

In Equation (14), L_i is the element length, A_i^* is the equivalent fracture area, and A_i is defined in Equation (10), being the subscript i is equal to l for the longitudinal elements or to d for the diagonal elements. The failure strain of the element, ε_r, can also be defined as $\varepsilon_r = k_r \varepsilon_p$, where k_r is a shape parameter that must be greater than or equal to 1.

The integral in Equation (14) represents the area under the constitutive model corresponding to the triangle area and computed as $\left(\frac{k_r \varepsilon_p \varepsilon_p E}{2}\right)$. Therefore, the shape parameter, k_r, is then given by

$$k_r = \frac{G_f}{{\varepsilon_p}^2 E}\left(\frac{A_i^*}{A_i}\right)\left(\frac{2}{L_i}\right) = d_{eq}\left(\frac{A_i^*}{A_i}\right)\left(\frac{2}{L_i}\right) \tag{15}$$

It is important to highlight that the shape parameter k_r depends on the material characteristic length, d_{eq}, as well as the discretization used in the simulation (remember that $A_i^*/A_i = 0.3474$). When the discretization changes, this shape parameter must be adjusted to ensure the correlation between the energy released during the fracture and the energy stored in the material.

Under compression, the element exhibits linear elastic behavior leading to rupture caused by Poisson's ratio, known as indirect tension. Brittle and quasi-brittle materials have this characteristic behavior, where the compressive strength is greater than the tensile strength [45,46].

The intrinsic inhomogeneity of the material can be represented by three-dimensional random fields, as proposed by [47]. The elastic modulus, density, and fracture energy can be modeled in this way, as explained in detail in [42,48]. Generally, the global results obtained with the LDEM are more sensible when considering the fracture energy, G_f, as a

random field. Therefore, by keeping the shape parameter k_r constant, the critical strain ε_p also becomes a random parameter. Notice that in Equation (13), E and d_{eq} are deterministic parameters, and then, ε_p inherits the random nature of the G_f, defined as a random field. It is crucial to represent the material heterogeneity as a random field of its properties independent of the LDEM discretization. As a result, the simulation outcomes remain consistent even if the LDEM discretization changes, as demonstrated in [48].

4. LDEM Implemented in Abaqus Environment

In this section, the LDEM-Abaqus version is presented. By implementing the standard LDEM (programmed in Fortran) into the Abaqus/Explicit 6.13 software [49], the Finite Element Method (FEM) and other tools available within Abaqus can be more easily utilized in conjunction with the LDEM. Thus, a wide range of problems can be simulated, as demonstrated in [41,42].

With the LDEM-Abaqus version, it becomes possible to model interactions between the LDEM and rigid surfaces or even FEM elements, creating a hybrid approach. In this case, the LDEM is applied to regions where it is crucial to model the transition from damage to fracture and from continuum to discontinuous, while the conventional FEM is used elsewhere. Another advantage of the LDEM-Abaqus version is the ability to use alternative constitutive models available in Abaqus 6.13 to simulate different material behaviors.

It is important to note that no custom subroutines were created to build the LDEM model within Abaqus. Instead, 3D truss elements (T3D2) with equivalent densities were used to model the LDEM elements (as discussed in Section 3.1), and a constitutive law available in the Abaqus 6.13 library was used to account for fracture energy and its variation (as mentioned in Section 3.2).

4.1. LDEM-Abaqus Description

In the LDEM, the continuum is represented by a regular three-dimensional arrangement of elements, with masses concentrated at their ends (half of the element's mass at each node), derived from the repetition of a basic module (Figure 1a). The mass of a solid cube of size $L \times L \times L$ (ρL^3) is distributed among the nodes in the LDEM representation, with half of the cube's mass allocated to the central node and the remaining mass distributed among the eight corner nodes. Consequently, each internal node has a lumped mass of ($\rho L^3/2$), while nodes located at the corners have a lumped mass of ($\rho L^3/16$).

The equivalent density of LDEM elements is determined using the mass balance equation at the central node:

$$\frac{1}{2}\rho L^3 = \frac{1}{2}(6)\rho_{eq} A_l L_l + \frac{1}{2}(8)\rho_{eq} A_d L_d \tag{16}$$

Here, the left-hand side of the equation represents the mass of the LDEM central node, while the right-hand side accounts for half the mass of each element connected to this node—specifically, six longitudinal elements and eight diagonal ones (with half of the element's mass lumped at each end).

When the basic LDEM module is repeated to model a body, some nodes may not be influenced by six longitudinal elements and eight diagonal ones, as described in Equation (16). In order to overcome this mass deficit, a mass of $\overline{m} = 0.5n\rho_{eq} A_l L$ is added to these nodes, where the number of missing longitudinal elements that reach the node is n. Figure 2a illustrates a body modeled with $3 \times 3 \times 2$ basic LDEM modules, detailing a face module and a corner module, where missing longitudinal elements can be observed (Figure 2b).

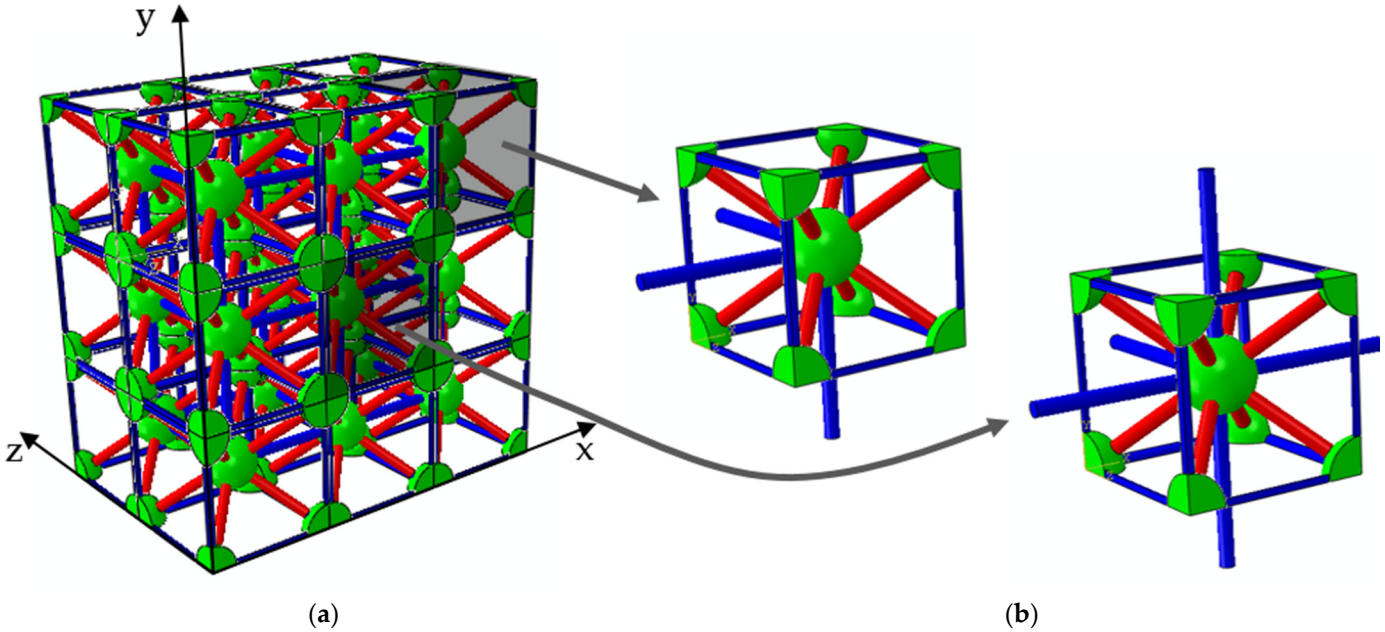

Figure 2. (**a**) Solid modeled with 3 × 3 × 2 LDEM basic cubic modules. (**b**) Details of modules on the corner and on the face of the solid model.

4.2. Constitutive Model

The LDEM bilinear constitutive law presented in Figure 1b is represented exactly within the Abaqus/Explicit 6.13 environment by the superposition of the linear elastic behavior that defines the loading branch plus another model to describe the softening branch. There are different options to represent the softening branch in Abaqus. One approach is to use the Brittle Cracking Constitutive Model [41], while another involves accounting for unloading with residual strains (where unloading does not return to the origin) using the Concrete Damaged Plasticity Model [42]. This work employs the first approach.

The brittle cracking constitutive model is a concrete failure model available in the Abaqus 6.13 library [49]. It accurately represents the LDEM bilinear constitutive law, which includes a bilinear relationship for tension and linear-elastic behavior for compression and facilitates the removal of broken elements during the simulation. The brittle behavior of concrete, considering the distributed cracks as discontinuities, supports this constitutive model. The material fracture energy in mode I (G_f) is used as a fracture parameter. Figure 3 depicts this model.

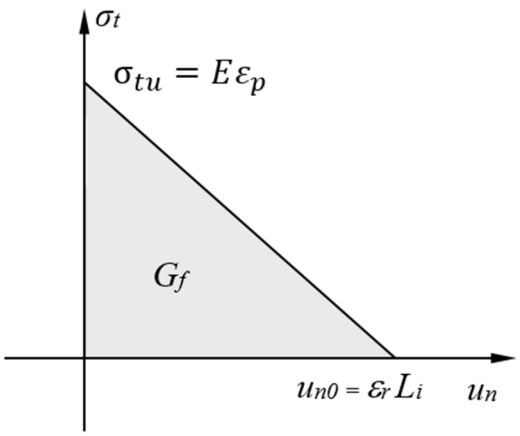

Figure 3. Brittle cracking model parameters.

The brittle cracking model available in Abaqus 6.13, shown in Figure 3, represents a curve as a function of the normal displacement (u_n) and the tensile stress (σ_{tu}). It is important to note that σ_t is obtained by dividing the load F by the cross-sectional areas of the elements presented in Equation (10). The normal displacement u_n is obtained by multiplying the strain by the element length, L_i. Then, the brittle cracking model is intricately connected to the constitutive law of the standard LDEM (Figure 1b), defined by the element failure strain (ε_r) and the maximum stress the element can withstand, which occurs when the element strain reaches ε_p. Beyond this strain, the elements begin to experience damage due to traction. The LDEM bilinear constitutive law parameters allow expressing the maximum stress as $\sigma_{tu} = E\varepsilon_p$.

Similar to the standard LDEM, mechanical properties such as mass density, Young's modulus, and fracture energy can be defined as random fields. These fields are characterized by their statistical distribution and spatial distributions, which are described by spatial correlation information.

More precisely, a given material property X for each element is herein assumed to be satisfactorily modeled by a Weibull probability distribution. The properties of this distribution are presented in Table 1, where β and γ are the scale and shape parameters, respectively.

Table 1. Characteristics of Weibull distribution used to describe the X material property's variation.

Weibull probability distribution	$F(X) = 1 - exp\left[-(X/\beta)^{\gamma}\right]$
Mean value	$\overline{X} = \beta[\Gamma(1 + 1/\gamma)]$
Standard deviation	$s_t = \beta\left[\Gamma(1 + 2/\gamma) - \Gamma^2(1 + 1/\gamma)\right]^{1/2}$

Note that $\Gamma(x) = \int_0^{\infty} t^{x-1}e^{-t}dt$ denotes the Gamma function.

To simulate pseudo-random values of X, the following formula was applied:

$$X = \beta[-\ln(1 - r)]^{1/\gamma} \tag{17}$$

Here, r is a random number uniformly distributed within the range (0, 1). Numerous routines are available for generating samples of r.

In this study, only the material fracture energy, G_f, is employed as a random variable. Its spatial correlation is characterized by a correlation length, which guarantees that this material property remains unaffected by the model discretization. For further details regarding this implementation, see [48].

5. Simulation of Size Effect on Rock Specimens

In this study, the failure of rock specimens of varying dimensions is simulated to analyze the cohesive fractal law behavior using the LDEM within the Abaqus environment. Three loading scenarios are numerically examined: tensile, flexural, and compressive tests.

Table 2 shows the material properties related to a rock material (granite) used on the three loading scenarios mentioned above. A 3D random field is used to model the fracture energy G_f, which is related to the module size L. Specifically, the probability distribution of G_f follows a Weibull function (see Table 1), with the mean value, coefficient of variation, and correlation length provided in Table 2. The correlation length represents the distance at which the fracture energy values in this random field become uncorrelated.

Square plates of 200 mm side with different correlation lengths, as presented in Figure 4, exemplify the above random field. Correlation length values (Lcx = Lcy) equal to 1.5 mm, 10 mm, 20 mm, and 40 mm are used.

It is important to point out that every simulation generates unique stress–strain or displacement curves due to the fact that the material's properties are randomly distributed. To obtain representative results, four simulations are conducted for specimens of each size on each loading scenario.

Table 2. Material properties and parameters utilized in the LDEM simulations.

Material Properties	Value
E (Young's modulus)	75 GPa
ρ (mass density)	2700 kg/m^3
ν (Poisson ratio)	0.25
d_{eq} (characteristic length of the material)	1.465 m
ε_p (mean elementary characteristic strain)	1.0878×10^{-4}
$\overline{G_f}$ (Mean fracture energy related to size L)	1300 N/m
CV (G_f) (coefficient of variation of G_f)	40%
L (basic LDEM module length)	5 mm

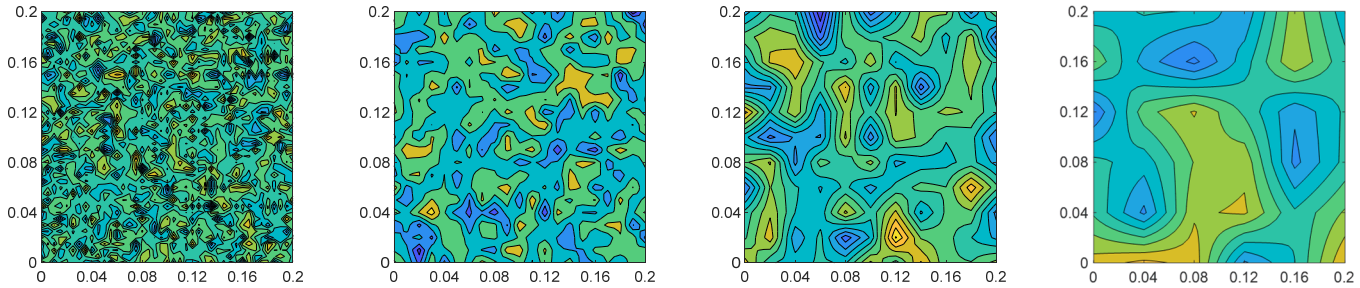

(**a**) (**b**) (**c**) (**d**)

Figure 4. The 2D G_f random fields when (**a**) $Lcx = Lcy = 1.5$ mm; (**b**) $Lcx = Lcy = 10$ mm; (**c**) $Lcx = Lcy = 20$ mm; and (**d**) $Lcx = Lcy = 40$ mm.

5.1. Rock Specimens Under Tensile Loading

The same set of rock specimens exploited by Kosteski et al. [18,19] are simulated now using the LDEM implemented in the Abaqus/Explicit 6.13 environment. For this work, simulations are conducted with side lengths b ranging from 50 to 750 mm. The specimens are fixed at the lower face, while the upper faces experience a monotonic increasing displacement with a strain rate of 0.1 s^{-1}. In order to achieve plane strain conditions, in all instances, the nodal displacements are restrained in the model thickness direction. The specimens are analyzed up to complete failure. The smallest specimen, with a side length of 50 mm, is modeled with an LDEM array of $10 \times 10 \times 1$ cubic modules with 1026 degrees of freedom (DOF). This is the smallest array that produces satisfactory results. At the same time, the largest specimen used in this study is the specimen with a side length of 750 mm, modeled with $150 \times 150 \times 1$ cubic modules with 204,306 DOF. The dimensions of the samples are presented in Table 3. Figure 5a shows the boundary condition and the layout of the specimens.

Table 3. LDEM's studied model's dimensions.

Specimen	1	2	3	4	5	6	7	8	9	10
Side b (mm)	50	75	100	150	200	250	300	400	500	750
Side b (modules)	10	15	20	30	40	50	60	80	100	150

The numerical simulations of the tensile test are performed by considering four correlation length values ($Lcx = Lcy$): 1.5 mm, 10 mm, 20 mm, and 40 mm. The smaller correlation length employed is equal to 1.5 mm, which is smaller than the basic module length. Therefore, each element has statistically independent values of G_f. This means that the properties of one element are not influenced by the properties of neighboring elements.

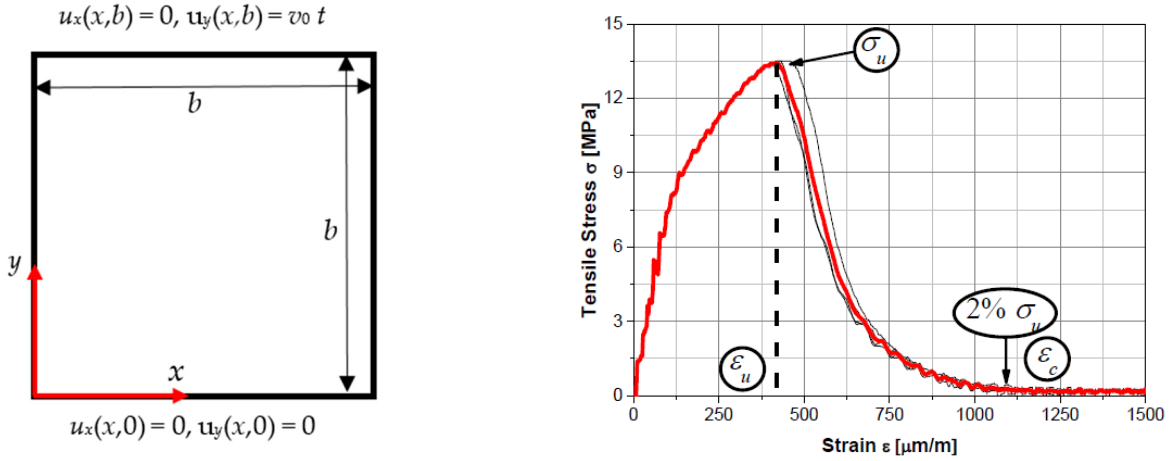

(**a**) (**b**)

Figure 5. (**a**) Model dimensions and boundary conditions; (**b**) tensile stress vs. strain of the four simulations of rock specimens with b = 200 mm, with the average curve in red.

Figure 5b presents the stress–strain curves resulting from all simulations (in black) of the specimen characterized by b = 0.20 m together with the average curve (in red). Figure 5b presents the key parameters characterizing the stress–strain curves: σ_u is the ultimate stress and ε_u its corresponding strain. Finally, the strain at which stress falls below 2% of the ultimate stress is defined as critical strain, ε_c. This notation is applicable to specimens with ductile behavior but also to specimens with brittle behavior. In the specimens when failure occurs in a brittle manner, the only complication is distinguishing the ultimate strain (strain at peak) from the critical strain, ε_c.

5.2. Rock Specimens Under Flexural Loading

In order to examine the size effect of rock specimens under flexural loading, three beams of varying dimensions (named small, medium, and large in the following) and proportional to each other, with a scale factor of 2.0 in all dimensions, are considered (see Table 4). For each configuration, four random fields of G_f are employed.

Table 4. Beam dimensions (modules) for rock samples under flexural loading.

Dimensions	Small	Medium	Large
L (mm)	200	400	800
S (mm)	150	300	600
b (mm)	25	50	100
t (mm)	15	30	60

Regarding the boundary conditions, the nodes on the left-hand side and on the right-hand side, both on the bottom face of the model, are constrained in the y direction, whereas on the nodes located at the center of the beam and on the upper face, a uniform vertical displacement is applied in the y direction (see Figure 6). In order to produce satisfactory results, the smallest LDEM array used to simulate the small beam consists of 3 × 5 × 40 cubic modules with 2736 DOF. At the same time, the large beam consists of 14 × 20 × 160 cubic modules with 252,219 DOF, thus constituting the largest specimen used in this loading scenario.

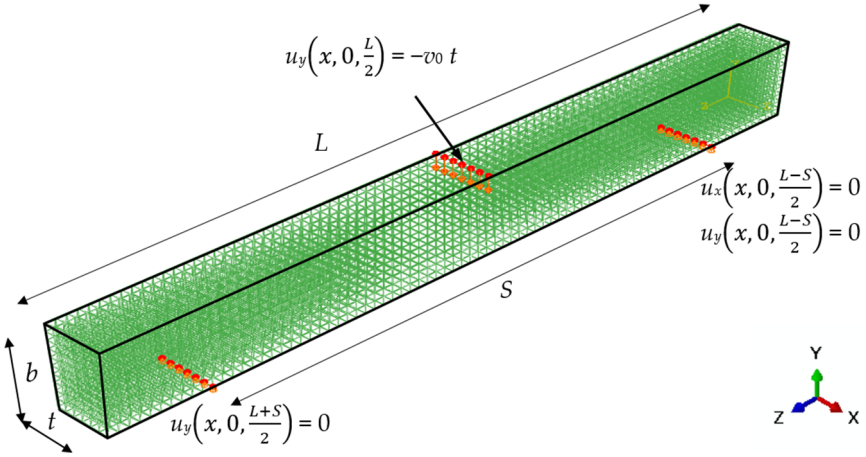

Figure 6. Model and boundary conditions for the medium specimen rock under flexural loading.

5.3. Rock Specimens Under Compressive Loading

In order to examine the size effect of rock specimens under compressive loading, cubic samples with 50 mm, 100 mm, and 200 mm sides are employed. Figure 7 illustrates the three cubic specimen sizes under consideration together with a representation of the LDEM mesh for the largest one.

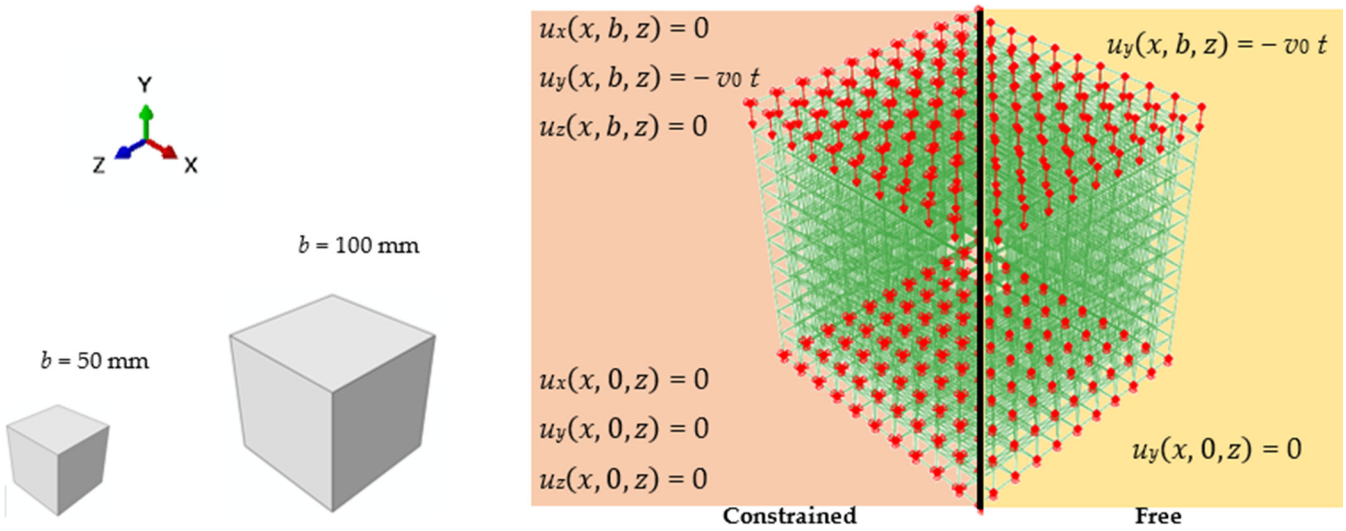

Figure 7. Cubic specimens considered together with details of LDEM discretization and types of boundary conditions: constrained and free.

The rock samples are analyzed by considering two different boundary conditions: constrained and free. In the constrained boundary condition, all nodes of the upper and down surfaces are fixed in the horizontal plane, that is on x and z directions (see Figure 7). In the free boundary condition, all nodes of the upper and down surfaces are free in the horizontal plane. In both conditions, a uniform vertical displacement is applied in the -y direction on the upper nodes and those on the down surface are fixed in that direction.

The smallest LDEM array consists in 10 × 10 × 10 cubic modules with 6993 DOF and is employed for the smallest (b = 50 mm) model. At the same time, when b = 200 mm the model consists in 40 × 40 × 40 cubic modules with 369,957 DOF, representing the largest cubic specimen employed in this analysis. It should be noted that models of larger sizes are not considered due to limitations in computational capacity.

Regarding the G_f random field, the numerical simulations of the compressive tests are performed by considering the same four correlation length values ($Lcx = Lcy$) employed in the case of the tensile scenario, that is 1.5 mm, 10 mm, 20 mm, and 40 mm.

6. Results and Discussion

6.1. Tensile Scale Effect

Table 5 shows the mean values of the parameters (see Figure 5b) obtained from the stress–strain curves for the specimens simulated with different sizes and with a correlation length equal to 1.5 mm. Table 5 also presents the mean values of the strain energy (E_S), kinetic energy (E_K), and the energy dissipated by damage (U_D). These values are referred to as the peak of stress (that is, at σ_u as shown in Figure 5b) and divided by the cross-section of the specimen ($b\ t$).

Table 5. Mean values of ultimate stress, ultimate strain (strain at the peak of stresses), and critical strain together with values of the kinetic, strain, and dissipated by damage energies per unit area measured at peak to each of the specimen sizes studied. In the table is also indicated +/− one standard deviation of each value.

b [mm]	σ_u [N/mm^2]	ε_u [μm/m]	ε_c [μm/m]	*At Peak Energy* [Nm/m^2]		
				E_K	E_S	U_D
50	13.46 ± 0.15	523 ± 39	4509 ± 204	0.8 ± 0.4	161 ± 8	75 ± 8
75	13.52 ± 0.11	456 ± 33	2807 ± 141	0.8 ± 0.4	232 ± 12	104 ± 10
100	13.42 ± 0.13	433 ± 24	2073 ± 85	0.9 ± 0.4	290 ± 14	126 ± 11
150	13.51 ± 0.09	428 ± 0	1418 ± 2	0.9 ± 0.4	435 ± 20	184 ± 15
200	13.47 ± 0.05	424 ± 13	1067 ± 26	1.0 ± 0.4	561 ± 22	229 ± 16
250	13.43 ± 0.09	421 ± 6	812 ± 14	1.0 ± 0.3	682 ± 29	272 ± 22
300	13.39 ± 0.02	412 ± 1	615 ± 29	0.9 ± 0.3	830 ± 32	352 ± 23
400	13.49 ± 0.04	414 ± 5	460 ± 15	1.0 ± 0.3	1138 ± 34	494 ± 29
500	13.47 ± 0.04	410 ± 6	457 ± 11	1.5 ± 0.5	1375 ± 39	545 ± 35
750	13.46 ± 0.05	402 ± 8	429 ± 7	2.2 ± 0.4	2019 ± 55	793 ± 43

The fractal exponent of tensile strength, d_σ, is defined as the slope of the bi-logarithmic plot of the normal strength versus the characteristic specimen size, b (see Figure 8a). This exponent quantifies the tensile scale effect. From this figure, a practical null scale effect is identified (d_σ = 0.002) as being the fractal tensile strength defined as σ_u^* = 13.586 MN/mm$^{1.998}$. Moreover, the variability of the values is considerable for the small specimens, as presented in Figure 8a; however, this variation decreases after b = 200 mm.

The fractal exponent of deformations, d_ε, can be determined by measuring the slope of the bi-logarithmic plot of the critical displacement, $w_u = \varepsilon_u b$, against the characteristic specimen size, b (Figure 8b). The fractal exponent and the fractal strain are defined at the peak displacement as $d_{\varepsilon u}$ = 0.04 and ε_u^* = 526 μm/m, respectively.

Finally, the variation in fracture energy with specimen size on the bi-logarithmic scale is plotted in order to compute the fracture energy fractal exponent, d_G (Figure 8c). To compute G_f, the energy balance method presented by Kosteski et al. [19] is employed. According to that method, the fracture energy is defined as the total energy at the peak stress, subtracting the energy dissipated by damage (U_D) at the same point. However, the kinetic energy is disregarded at the point of maximum stress (see Table 5). Therefore, the strain energy per unit of area measured at the peak stress would be equivalent to the "fracture energy", which represents the energy released before the onset of damage nucleation. From Figure 8c, the fractal exponent is d_G = 0.96 and, therefore, the fractal fracture energy is $G_f^* \approx 3.58$ Nm/m$^{2.96}$.

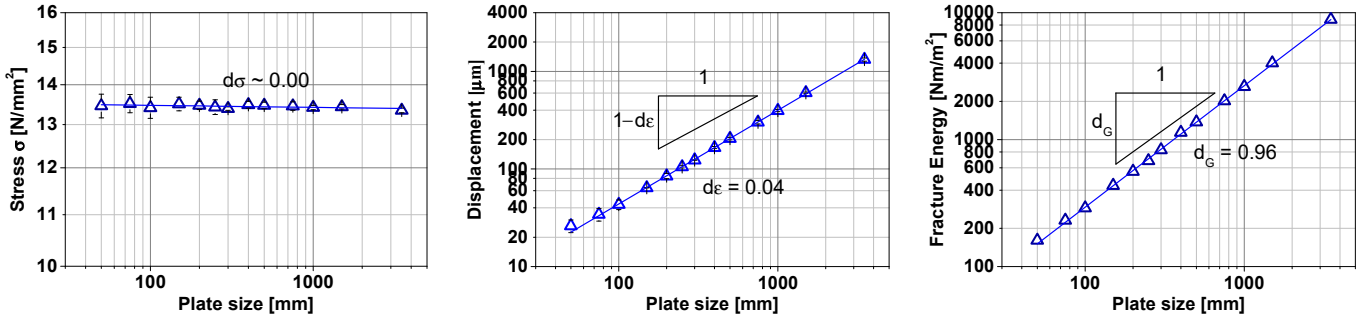

(**a**) (**b**) (**c**)

Figure 8. Fractal scale effect on the (**a**) tensile strength σ_u, (**b**) critical strain ε_u, and (**c**) fracture energy for rocks under tensile loading. The mean values (blue triangles) and bar with ±1 standard deviation are also indicated. The fitting lines have been obtained through the use of the least squares method.

Carpinteri's cohesive fractal law, as detailed in Equation (5), states that the three fractal exponents added must equal 1.0 [21,22,24,27,28,50]. This statement has been confirmed in simulations carried out with the LDEM, which are in full agreement with fractal scale effect theory.

It is worth noting that in Kosteski et al. [18], the same set of specimens was analyzed by employing the standard LDEM. In that work, the authors classified the structural response using Carpinteri's brittleness number, *s*, as brittle, ductile, or brittle-to-ductile transition behavior. This work shows a good agreement between the results obtained from LDEM simulations and those obtained from experimental data in the technical literature. Therefore, it is evident that the method can accurately capture the behavior of structures and is in accordance with the principles of classical structural mechanics.

Figure 9 shows the influence of the correlation length (*Lcx* = *Lcz*) of the random field fracture energy on the scaling exponents of tensile strength, critical strain, and fracture energy. More precisely, the correlation length, which was previously analyzed in Figure 8, is equal to 1.5 mm, a value that is typical for small-grained hard rock but rare in concretes. Therefore, the following correlation lengths are considered: 10 mm, 20 mm, and 40 mm.

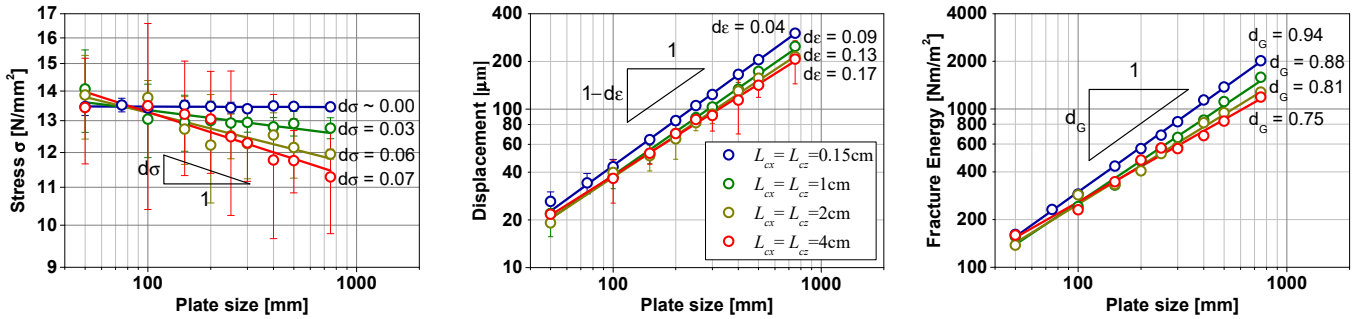

(**a**) (**b**) (**c**)

Figure 9. Influence of the correlation length (*Lcx* = *Lcz*) of the size effect on the (**a**) ultimate tensile strength, (**b**) ultimate strain, and (**c**) fracture energy for rock samples under tensile loading. The mean values (circles) and bar with ±1 standard deviation are also indicated. The fitting lines have been obtained through the use of the least squares method.

From Figure 9, it is possible to note that the increase in the correlation length leads to an increase in the fractal exponent of the tensile strength and strain. In contrast, the fractal exponent of the fracture energy reduces with the correlation length. Notably, the sum of the three fractal exponents is approximately 1.0, which aligns with the fractal cohesive law theory as well. Moreover, Figure 9 demonstrates that smaller specimens do not always produce accurate results and that result dispersion increases with the correlation length.

The smaller specimens have a suboptimal mesh discretization, particularly the specimen modeled with only 10 × 10 LDEM basic modules.

Table 6 provides a summary of the fractal exponents obtained from the simulations shown in Figure 9. It is evident that for all cases analyzed, the sum of the three fractal exponents is close to one. This is a reasonable result, given that the three fractal exponents, stress, strain, and fracture energy, are derived from the maximum stress, characterize the strain distribution at the peak, and describe the damage distribution along the specimen, respectively, all at stress peaks.

Table 6. Mean values of the true tensile strength, strain, and fracture energy together with values of the fractal exponents and the sum of them for each correlation length examined.

$L_{cx} = L_{cz}$	σ_u^*	d_σ	ε_u^*	d_ε	G_f^*	$\mathbf{d_G}$	$d_\sigma + d_\varepsilon + d_G$
1.5 mm	13.502	0.00	0.546	0.05	3.920	0.94	0.99
10 mm	15.226	0.03	0.574	0.09	4.468	0.88	1.00
20 mm	17.250	0.06	0.673	0.13	5.976	0.81	1.00
40 mm	18.583	0.07	0.844	0.17	8.318	0.75	0.99

These fractal values are associated with the microstructure of the specimen. When there is greater heterogeneity (a smaller correlation length, *Lc*, relative to the specimen size), the properties show more variability, and strain tends to diffuse. In this case, the fractal fracture energy is released almost uniformly throughout the specimen. When *Lc* increases, areas with minimal properties tend to concentrate displacements, and these areas release more fracture energy. Therefore, the three exponents are interdependent at this point.

6.2. Flexural Scale Effect

Figure 10a shows the global behavior in terms of flexural load versus the mid-span deflection curves obtained in the simulations. The correlation length (*Lcx* = *Lcz*) of the G_f random field is assumed to be equal to 1.5 mm. From Figure 10a, it is possible to compute the flexural strength using Equation (18):

$$\sigma = \frac{3FS}{2tb^2} \tag{18}$$

where the values of S, t, and b are defined in Table 4 and Figure 6.

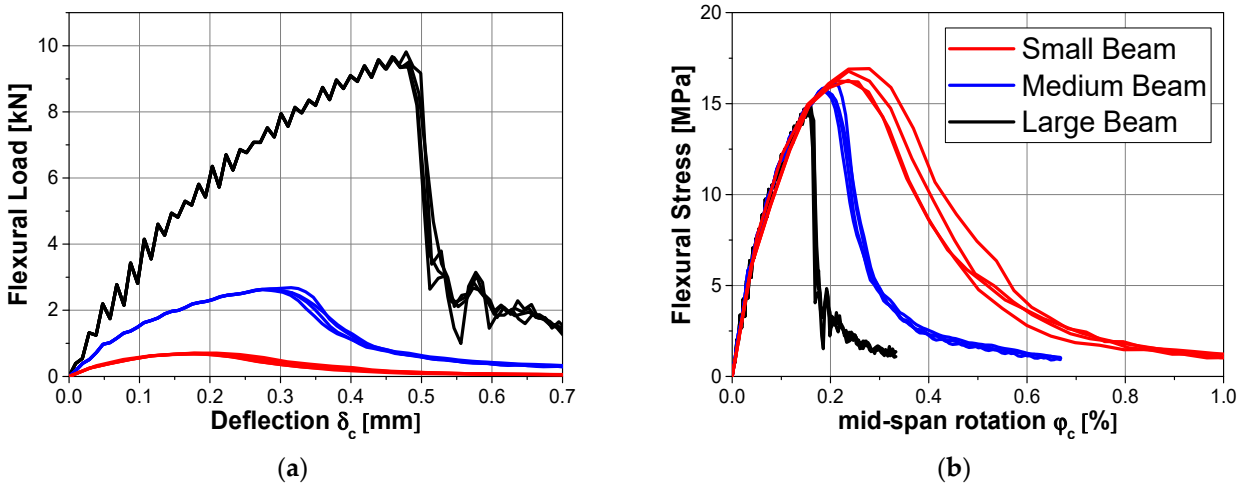

(**a**) (**b**)

Figure 10. (**a**) Flexural load versus mid-span deflection curves and (**b**) flexural stress versus localized rotation at the beam mid-span for the three beam sizes considered (see Table 3).

Under flexural loading, the fractal kinematic parameter considered, which has the same meaning as the critical strain in a tensile test, is the localized rotation at the beam mid-span. This parameter at the point of failure (δ_c) is defined as follows:

$$\varphi_c = \frac{\delta_c}{S/2} \tag{19}$$

The flexural stress–rotation curves obtained in the numerical simulations are shown in Figure 10b.

As defined in [38,39], the area under the curve flexural load versus deflection (F–δ_c) is defined as the dissipated energy (W). The flexural fracture energy is the energy dissipated at the peak flexural load divided by the cross-section of the beam.

Figure 11 presents the scale effect of (a) flexural strength, (b) mid-span rotation, and (c) fracture energy at the peak flexural load of the simulated beams submitted to three-point bending testing.

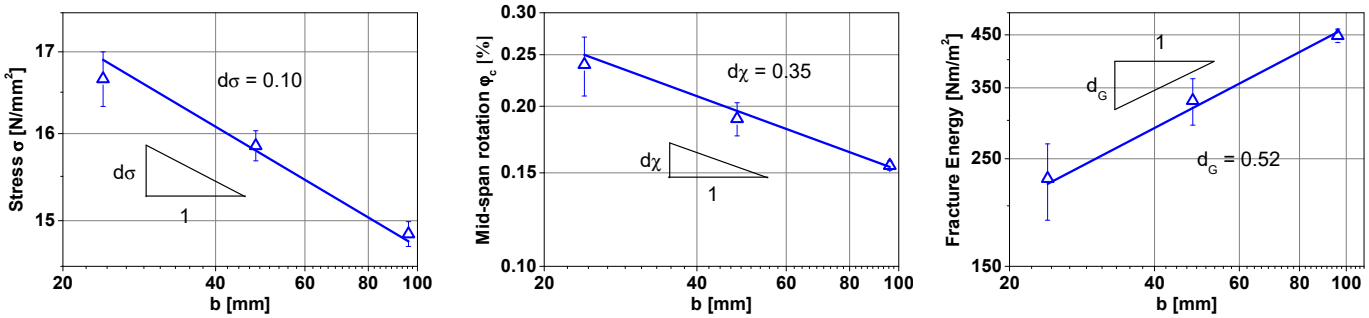

Figure 11. Fractal scale effect on the (**a**) flexural strength, (**b**) critical strain, and (**c**) flexural fracture energy for rocks under flexural loading. The mean values (blue triangles) and bar with ±1 standard deviation are also indicated. The fitting lines have been obtained through the use of the least squares method.

The sum of the flexural fractal exponents, d_σ = 0.10, $d\chi$ = 0.35, and d_G = 0.52, is also close to 1. Therefore, the LDEM simulations capture the size effect on rocks under three-point bending tests using Carpinteri's cohesive (flexural) fractal law.

6.3. Compressive Scale Effect

Following the methodology employed in Section 5.1, in order to compute the fractal tensile exponents, the fractal scale effects on the cubic samples under compression are here examined. In this first analysis, the effect of the two different boundary conditions (see Section 5.3) on the scaling exponents is investigated by considering a fixed correlation length equal to 1.5 mm.

Figure 12a presents the compressive stress–strain curves obtained with the simulations, while Figure 12b presents the results expressing the displacement.

From the stress–strain curves (Figure 12a), the size effect on the normal compressive strength, strain related to maximum compressive stress, and fracture energy is obtained (see Figure 13). The coefficient of variation of the results is less than 2.5% in the fracture energy, 2.7% in the strain, and 5.4% in the fracture energy. Consequently, these values are not visible in the plot of Figure 13.

Table 7 summarizes the fractal exponents obtained from the numerical simulations of the compression tests together with the true compressive strength (in $MN/mm^{2-d\sigma}$), strain (in $\mu m/m^{1-d\varepsilon}$), and fracture energy (in Nm/m^{2+dG}). It can be observed that the sum of the three fractal exponents is close to 1.0 for the constrained boundary condition and equal to 1.8 for the free one. The results for the free boundary condition apparently do not agree with the cohesive fractal law. This specific case must be better studied to

guarantee these results with comprehensive size dimensions, since it is beyond the scope of this work.

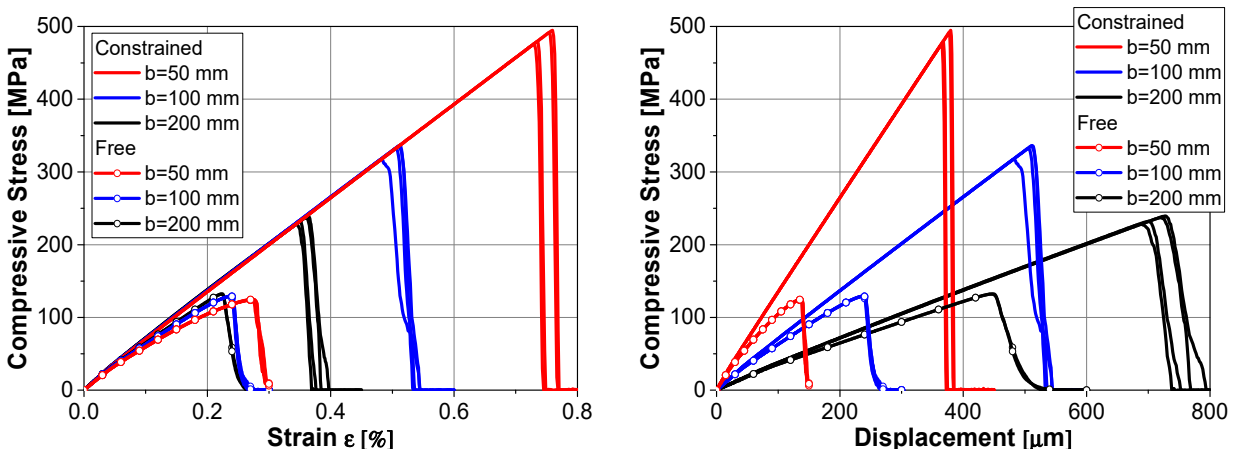

Figure 12. (**a**) Compressive stress–strain curves and (**b**) compressive stress–displacement curves for the cubic samples of 50 mm, 100 mm, and 200 mm considering the constrained and free boundary conditions.

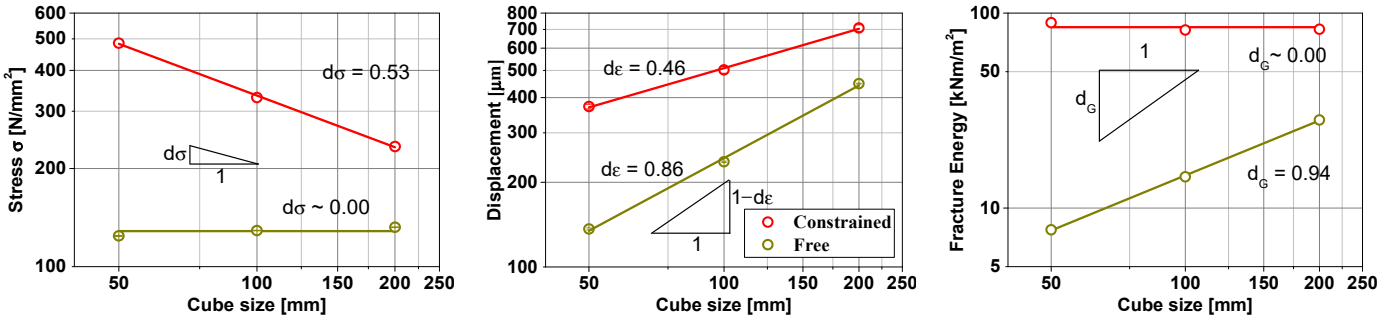

Figure 13. Fractal scale effect on the (**a**) compressive strength, (**b**) critical strain, and (**c**) fracture energy for rocks under compressive loading considering the constrained and free boundary conditions. The mean values (circles) and bar with ±1 standard deviation are also indicated. The fitting lines have been obtained through the use of the least squares method.

Table 7. Mean values of the true compressive strength, strain, and fracture energy together with values of the fractal exponents and the sum of them for each boundary condition examined.

Boundary Conditions	σ_u^*	d_σ	ε_u^*	d_ε	G_f^*	d_G	$d_\sigma + d_\varepsilon + d_G$
Constrained	3794	0.53	60.21	0.46	84.54	0.00	0.99
Free	129	0.00	4.68	0.86	0.20	0.94	1.80

The compressive strengths reported in the numerical simulations for the constrained boundary condition are considerably higher than the expected values for rocks. For example, the granite has a compressive strength ranging from 90 to 210 N/mm^2 [51,52]. However, when the free boundary condition is employed, the true compressive strength is approximately 130 N/mm^2, regardless of the cube size. These values are more aligned with the actual values observed in rocks.

Figure 14 illustrates the failure configuration as reported by the numerical simulations for both boundary conditions. The broken elements are plotted in red to facilitate a more straightforward interpretation.

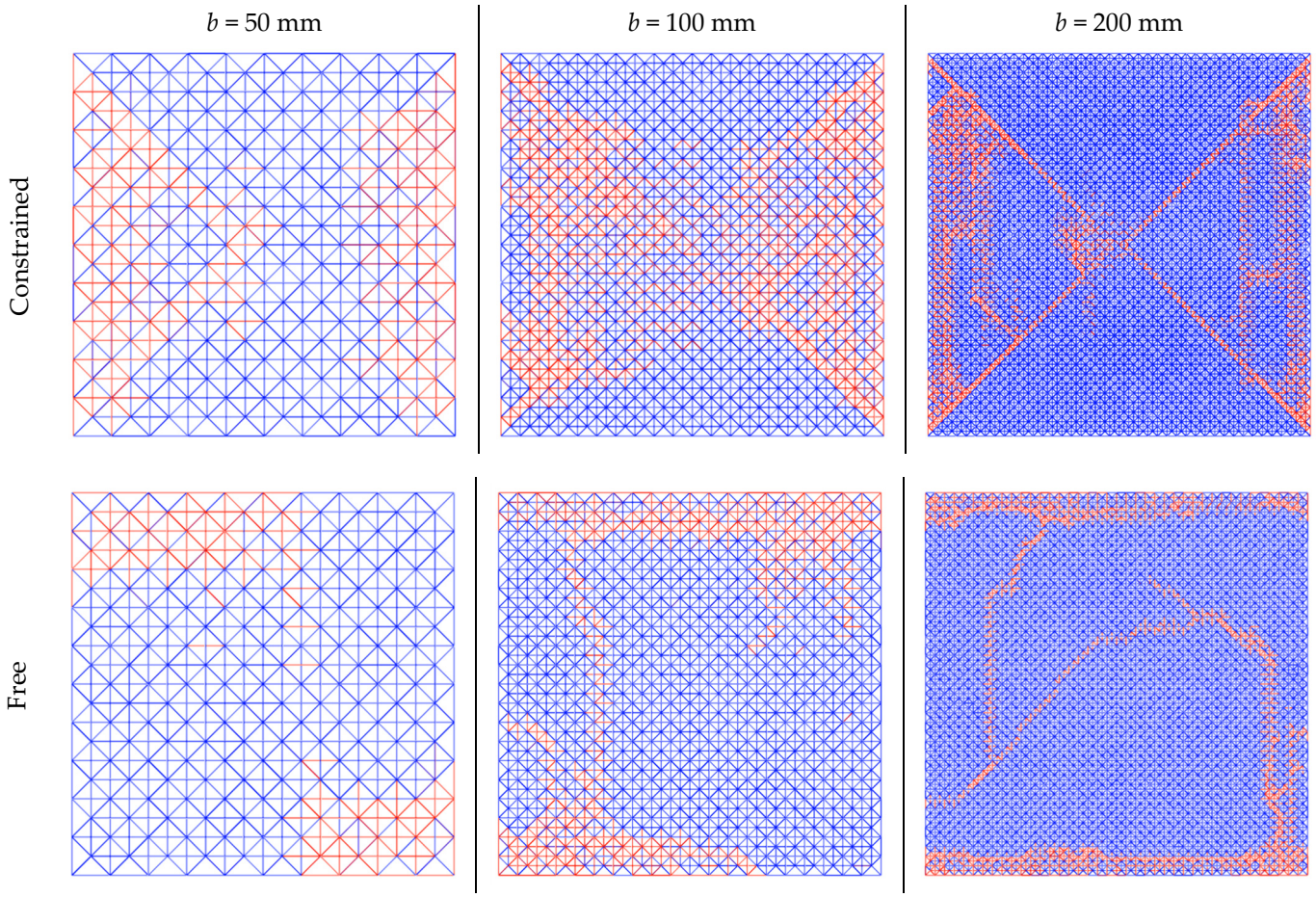

Figure 14. Representative failure configurations reported by the numerical simulations for different cube sizes, considering the constrained boundary condition and the free boundary condition. The broken elements are in red.

It can be observed that the simulation with constrained boundary conditions consistently results in a bi-cone or hourglass failure pattern. In contrast, the free boundary condition produces a more intricate crack pattern, with cracks initially forming on the surface subjected to the load and subsequently propagating vertically. The results of the failure configuration are in accordance with the values of the fractal fracture energy exponent. More precisely, for the constrained boundary conditions, which report a fractal exponent of fracture energy $d_G = 0$ ($\Delta G = 2 + d_G$), a localized fracture on a plane is observed, with the damaged elements concentrated in a surface at 45°, forming the hourglass shape. On the other hand, when the free boundary condition is employed, the damaged elements are distributed throughout the volume; that is, $\Delta G = 2 + 0.94$.

Figure 15 shows the influence of the correlation length ($Lcx = Lcz$) of the random field fracture energy on the scaling exponents of compressive strength, critical strain, and fracture energy for the constrained boundary condition only. More precisely, the following correlation lengths are considered: 1.5 mm, 10 mm, 20 mm, and 40 mm. The results show that similar values of fractal exponent are obtained regardless of the correlation length employed. Moreover, the dispersion of results increases with the correlation length, exhibiting the greatest dispersion when $Lcx = Lcy = 40$ mm. The fractal invariant (or normalized) values exhibit a slight decline with the correlation length employed. In other words, while the values decrease with the correlation length used, the inclination of the curves on the bi-logarithmic scale remains unchanged.

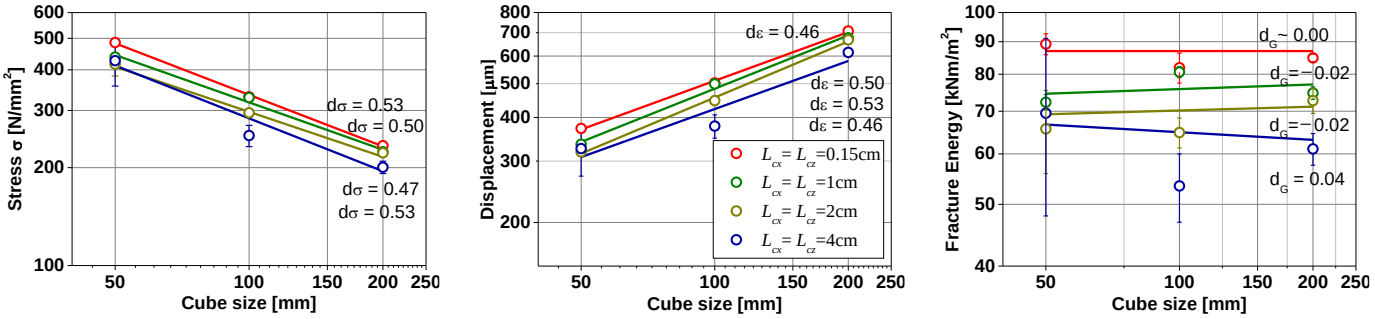

(**a**) (**b**) (**c**)

Figure 15. Fractal scale effect on the (**a**) compressive strength, (**b**) critical strain, and (**c**) fracture energy for rocks under compressive loading considered by varying the correlation length of the random field. The mean values (circles) and bar with ±1 standard deviation are also indicated. The fitting lines have been obtained through the use of the least squares method.

It can be observed that the sum of the fractal exponents is approximately 1.0 in this loading scenario, irrespective of the correlation length employed in the simulations. The fractal exponents of compressive strength and strain are both around 0.5, in accordance with the linear elastic fracture mechanics (LEFM) prediction. The fracture energy exponent, measured in a manner analogous to that employed in tensile loading, is 0 or negative.

7. Conclusions

This study demonstrates the size effect on rocks under tensile, flexural, and compressive loading using the Lattice Discrete Element Method, confirming that the findings align with Carpinteri's fractal cohesive law. Based on the results reported above, the following conclusions can be drawn:

- In the numerical simulation of tensile tests, the fractal cohesive law effectively represents the scale effect, with fractal exponents changing according to the correlation length of the random field fracture energy. As this length increases, the fractal exponents for tensile strength and strain also increase, resulting in greater dispersion of the results.
- Regarding the simulations of flexural tests, the LDEM was also able to capture the size effect, with smaller models showing more variability in the results, emphasizing the need for larger specimen simulations.
- In LDEM models subjected to compressive loading, the boundary conditions strongly influence the results; when the boundaries are constrained, the fractal exponents' sum tends to be around 1.0, whereas in the case of free boundary conditions, the results exhibit a greater degree of variability, with the fractal exponents' sum approaching 2.0.
- Notice that in the numerical method used (LDEM), a simple elementary constitutive law (bilinear) has been selected to reduce the number of parameters that need to be defined and to facilitate their interpretation. This approach enables the capture of several aspects of the cohesive fractal law proposed by Carpinteri. Thus, this feature is an important consideration in the LDEM that should be taken into account.

The next stage of this research is to investigate the relationship between the fracture pattern and the cohesive fractal law.

Author Contributions: Conceptualization, L.E.K. and L.F.F.; methodology, L.E.K. and L.F.F.; software, L.E.K., L.F.F. and M.M.C.; validation, L.E.K., L.F.F. and M.M.C.; formal analysis, L.E.K., L.F.F., M.M.C., C.B., I.I., J.X. and G.L.; data curation, M.M.C. and C.B.; writing—original draft preparation, M.M.C. and C.B.; writing—review and editing, L.E.K., L.F.F., I.I., J.X. and G.L.; supervision, L.E.K., L.F.F., I.I., J.X. and G.L. All authors have read and agreed to the published version of the manuscript.

Funding: The authors acknowledge the Coordination for the Improvement of Higher Level of Education Personnel (CAPES), the Brazilian National Council for Scientific and Technological Development (CNPq), and the National Natural Science Foundation of China for their financial support of this work. Moreover, the sponsorship was guaranteed with basic research funds provided by Politecnico di Torino (Italy).

Data Availability Statement: The original contributions presented in the study are included in the article; further inquiries can be directed to the corresponding author.

Conflicts of Interest: The authors declare no conflicts of interest.

References

1. Krajcinovic, D.; Vujosevic, M. Intrinsic failure modes of brittle materials. *Int. J. Solids Struct.* **1998**, *35*, 2487–2503. [CrossRef]
2. Krajcinovic, D. Damage mechanics. *Mech. Mater.* **1989**, *8*, 117–197. [CrossRef]
3. Gross, D.; Seelig, T. *Fracture Mechanics: With an Introduction to Micromechanics*; Springer: Cham, Switzerland, 2006; Volume 53.
4. Xu, X.-P.; Needleman, A. Numerical simulations of fast crack growth in brittle solids. *J. Mech. Phys. Solids* **1994**, *42*, 1397–1434. [CrossRef]
5. Huang, Y.; Natarajan, S.; Zhang, H.; Guo, F.; Xu, S.; Zeng, C.; Zheng, Z. A CT image-driven computational framework for investigating complex 3D fracture in mesoscale concrete. *Cem. Concr. Compos.* **2023**, *143*, 105270. [CrossRef]
6. Belytschko, T.; Black, T. Elastic crack growth in finite elements with minimal remeshing. *Int. J. Numer. Methods Eng.* **1999**, *45*, 601–620. [CrossRef]
7. Francfort, G.A.; Marigo, J.J. Revisiting brittle fracture as an energy minimization problem. *J. Mech. Phys. Solids* **1998**, *46*, 1319–1342. [CrossRef]
8. Ambati, M.; Gerasimov, T.; De Lorenzis, L. A review on phase-field models of brittle fracture and a new fast hybrid formulation. *Comput. Mech.* **2015**, *55*, 383–405. [CrossRef]
9. Wu, J.-Y.; Yao, J.-R.; Le, J.-L. Phase-field modeling of stochastic fracture in heterogeneous quasi-brittle solids. *Comput. Methods Appl. Mech. Eng.* **2023**, *416*, 116332. [CrossRef]
10. Silling, S.A. Reformulation of elasticity theory for discontinuities and long-range forces. *J. Mech. Phys. Solids* **2000**, *48*, 175–209. [CrossRef]
11. Niazi, S.; Chen, Z.; Bobaru, F. Crack nucleation in brittle and quasi-brittle materials: A peridynamic analysis. *Theor. Appl. Fract. Mech.* **2021**, *112*, 102855. [CrossRef]
12. Li, S.; Lu, H.; Jin, Y.; Sun, P.; Huang, X.; Bie, Z. An improved unibond dual-parameter peridynamic model for fracture analysis of quasi-brittle materials. *Int. J. Mech. Sci.* **2021**, *204*, 106571. [CrossRef]
13. Hobbs, M.; Dodwell, T.; Hattori, G.; Orr, J. An examination of the size effect in quasi-brittle materials using a bond-based peridynamic model. *Eng. Struct.* **2022**, *262*, 114207. [CrossRef]
14. Benkemoun, N.; Hautefeuille, M.; Colliat, J.-B.; Ibrahimbegovic, A. Failure of heterogeneous materials: 3D meso-scale FE models with embedded discontinuities. *Int. J. Numer. Methods Eng.* **2010**, *82*, 1671–1688. [CrossRef]
15. Nikolic, M.; Ibrahimbegovic, A.; Miscevic, P. Brittle and ductile failure of rocks: Embedded discontinuity approach for representing mode I and mode II failure mechanisms. *Int. J. Numer. Methods Eng.* **2015**, *102*, 1507–1526. [CrossRef]
16. Nikolić, M.; Karavelić, E.; Ibrahimbegovic, A.; Miščević, P. Lattice Element Models and Their Peculiarities. *Arch. Comput. Methods Eng.* **2018**, *25*, 753–784. [CrossRef]
17. Rios, R.D.; Riera, J.D. Size effects in the analysis of reinforced concrete structures. *Eng. Struct.* **2004**, *26*, 1115–1125. [CrossRef]
18. Kosteski, L.E.; Iturrioz, I.; Lacidogna, G.; Carpinteri, A. Size effect in heterogeneous materials analyzed through a lattice discrete element method approach. *Eng. Fract. Mech.* **2020**, *232*, 107041. [CrossRef]
19. Kosteski, L.E.; Iturrioz, I.; Friedrich, L.F.; Lacidogna, G. A study by the lattice discrete element method for exploring the fractal nature of scale effects. *Sci. Rep.* **2022**, *12*, 16744. [CrossRef]
20. Carpinteri, A. Scaling laws and renormalization groups for strength and toughness of disordered materials. *Int. J. Solids Struct.* **1994**, *31*, 291–302. [CrossRef]
21. Carpinteri, A.; Chiaia, B.; Cornetti, P. A scale-invariant cohesive crack model for quasi-brittle materials. *Eng. Fract. Mech.* **2002**, *69*, 207–217. [CrossRef]
22. Carpinteri, A.; Chiaia, B. Multifractal scaling laws in the breaking behaviour of disordered materials. *Chaos Solitons Fractals* **1997**, *8*, 135–150. [CrossRef]
23. Carpinteri, A.; Ferro, G. Size effects on tensile fracture properties: A unified explanation based on disorder and fractality of concrete microstructure. *Mater. Struct.* **1994**, *27*, 563–571. [CrossRef]
24. Carpinteri, A.; Chiaia, B. Multifractal nature of concrete fracture surfaces and size effects on nominal fracture energy. *Mater. Struct.* **1995**, *28*, 435–443. [CrossRef]
25. Carpinteri, A.; Corrado, M.; Lacidogna, G. Three different approaches for damage domain characterization in disordered materials: Fractal energy density, b-value statistics, renormalization group theory. *Mech. Mater.* **2012**, *53*, 15–28. [CrossRef]
26. Mandelbrot, B.B.; Wheeler, J.A. The Fractal Geometry of Nature. *Am. J. Phys.* **1983**, *51*, 286–287. [CrossRef]

27. Carpinteri, A. Fractal nature of material microstructure and size effects on apparent mechanical properties. *Mech. Mater.* **1994**, *18*, 89–101. [CrossRef]
28. Carpinteri, A.; Chiaia, B.; Invernizzi, S. Three-dimensional fractal analysis of concrete fracture at the meso-level. *Theor. Appl. Fract. Mech.* **1999**, *31*, 163–172. [CrossRef]
29. Carpinteri, A.; Cornetti, P.; Puzzi, S. Scaling Laws and Multiscale Approach in the Mechanics of Heterogeneous and Disordered Materials. *Appl. Mech. Rev.* **2006**, *59*, 283–305. [CrossRef]
30. Carpinteri, A.; Ferro, G. Scaling behaviour and dual renormalization of experimental tensile softening responses. *Mater. Struct.* **1998**, *31*, 303–309. [CrossRef]
31. van Vliet, M.R.A.; van Mier, J.G.M. Experimental investigation of size effect in concrete and sandstone under uniaxial tension. *Eng. Fract. Mech.* **2000**, *65*, 165–188. [CrossRef]
32. Strength and toughness in disordered materials: Complete and incomplete similarity. In *Size-Scale Effects in the Failure Mechanisms of Materials and Structures*, 1st ed.; CRC Press: Boca Raton, FL, USA, 2002; pp. 17–40. [CrossRef]
33. Carpinteri, A.; Corrado, M. An extended (fractal) Overlapping Crack Model to describe crushing size-scale effects in compression. *Eng. Fail. Anal.* **2009**, *16*, 2530–2540. [CrossRef]
34. Blanks, R.F.; Mcnamara, C.C. Mass Concrete Tests In Large Cylinders. *ACI J. Proc.* **1935**, *31*, 280–303. [CrossRef]
35. Xu, J.; He, X. Size effect on the strength of a concrete member. *Eng. Fract. Mech.* **1990**, *35*, 687–695. [CrossRef]
36. Ferro, G.; Carpinteri, A. Effect of specimen size on the dissipated energy density in compression. *J. Appl. Mech. Trans. ASME* **2008**, *75*, 041003. [CrossRef]
37. Van Mier, J.G.M.; Shah, S.P.; Arnaud, M.; Balayssac, J.P.; Bascoul, A.; Choi, S.; Dasenbrock, D.; Ferrara, G.; French, C.; Gobbi, M.E.; et al. Strain-softening of concrete in uniaxial compression. *Mater. Struct. Constr.* **1997**, *30*, 195–209. [CrossRef]
38. Carpinteri, A.; Accornero, F. Rotation Versus Curvature Fractal Scaling in Bending Failure. *Phys. Mesomech.* **2019**, *22*, 46–51. [CrossRef]
39. Lacidogna, G.; Piana, G.; Accornero, F.; Carpinteri, A. Multi-technique damage monitoring of concrete beams: Acoustic Emission, Digital Image Correlation, Dynamic Identification. *Constr. Build. Mater.* **2020**, *242*, 118114. [CrossRef]
40. Riera, J.D. Local effects in impact problems on concrete structures. In Proceedings of the Conference on Structural Analysis and Design of Nuclear Power Plants, Porto Alegre, Brazil, 3–5 October 1984.
41. da Silva, G.S.; Kosteski, L.E.; Iturrioz, I. Analysis of the failure process by using the Lattice Discrete Element Method in the Abaqus environment. *Theor. Appl. Fract. Mech.* **2020**, *107*, 102563. [CrossRef]
42. Eduardo Kosteski, L.; Iturrioz, I.; Ronchei, C.; Scorza, D.; Zanichelli, A.; Vantadori, S. Experimental and combined finite-discrete element simulation of the fracture behaviour of a rigid polyurethane foam. *Eng. Fract. Mech.* **2024**, *296*, 109818. [CrossRef]
43. Bathe, K. *Finite Element Procedures*, 2nd ed.; Prentice Hall: Hoboken, NJ, USA, 2014.
44. Hillerborg, A.; Modéer, M.; Petersson, P.E. Analysis of crack formation and crack growth in concrete by means of fracture mechanics and finite elements. *Cem. Concr. Res.* **1976**, *6*, 773–781. [CrossRef]
45. Kupfer, H.; Hilsdorf, H.K.; Rusch, H. Behavior of Concrete Under Biaxial Stresses. *Am. Concr. Inst. J.* **1969**, *66*, 656–666. [CrossRef]
46. Dominguez, N.; Brancherie, D.; Davenne, L.; Ibrahimbegović, A. Prediction of crack pattern distribution in reinforced concrete by coupling a strong discontinuity model of concrete cracking and a bond-slip of reinforcement model. *Eng. Comput.* **2005**, *22*, 558–582. [CrossRef]
47. Shinozuka, M.; Deodatis, G. Simulation of stochastic processes by spectral representation. *Appl. Mech. Rev.* **1991**, *44*, 191–204. [CrossRef]
48. Puglia, V.B.; Kosteski, L.E.; Riera, J.D.; Iturrioz, I. Random field generation of the material properties in the lattice discrete element method. *J. Strain Anal. Eng. Des.* **2019**, *54*, 236–246. [CrossRef]
49. Dassault Systems Simula Coorporation. *Abaqus 6.13—ABAQUS Analysis User's Guide*; Dassault Systems Simula Coorporation: Johnston, RI, USA, 2013.
50. Carpinteri, A.; Lacidogna, G.; Niccolini, G. Fractal analysis of damage detected in concrete structural elements under loading. *Chaos Solitons Fractals* **2009**, *42*, 2047–2056. [CrossRef]
51. Yun, X.; Mitri, H.S.; Yang, X.; Wang, Y. Experimental investigation into biaxial compressive strength of granite. *Int. J. Rock Mech. Min. Sci.* **2010**, *47*, 334–341. [CrossRef]
52. Armaghani, D.J.; Mamou, A.; Maraveas, C.; Roussis, P.C.; Siorikis, V.G.; Skentou, A.D.; Asteris, P.G. Predicting the unconfined compressive strength of granite using only two non-destructive test indexes. *Geomech. Eng.* **2021**, *25*, 317–330. [CrossRef]